

Early Stages of Protostellar Disk Evolution: A Link to the Initial Cloud Core

MAJD NOEL,^{1,2} RAHUL KHANNA,¹ SHAHRAM ABBASSI,¹ SAMI DIB,³ AND SHANTANU BASU^{1,2}

¹*Department of Physics and Astronomy, University of Western Ontario, London, Ontario N6A 3K7, Canada*

²*Canadian Institute for Theoretical Astrophysics, University of Toronto, 60 Saint George St., Toronto, ON M5S 3H8, Canada*

³*Max Planck Institute for Astronomy, Königstuhl 17, D-69117, Heidelberg, Germany*

ABSTRACT

We study the structure and evolution of the very early protostellar disk (“protodisk”) just after protostar formation, where disk self-gravity dominates and the stellar contribution is dynamically minor. The disk redistributes angular momentum outward through outflows and gravitational torques, thereby helping to resolve the angular momentum problem of star formation. We develop a self-similar model and carry out a parameter study that examines disk stability as a function of the key drivers of early evolution, notably the infall rate from the envelope and the strength of the gravitational torques. The mass infall rate onto the disk is estimated to be that from the collapse of a Bonnor-Ebert sphere. Our results indicate that protostellar disks that form from more unstable initial cores are more likely to be Toomre-unstable. We also find that the specific angular momentum of young protostellar disks lie in the range 10^{19} – 10^{20} cm² s^{−1}. We find distinct power-law profiles of physical quantities in the protodisk stage, including a rotation velocity profile that is shallower than the Keplerian profile that would be established at a later stage. As a rough validity window, our assumptions are most secure during the first $\lesssim 2 \times 10^3$ yr after protostar formation and may plausibly extend to $\sim (0.5\text{--}1) \times 10^4$ yr under weak magnetic braking and strong infall.

Keywords: Star formation (1569) — Stellar winds (1636) — Circumstellar disks (235) — Hydrodynamics (1963) — Gravitational collapse (662) — Interstellar medium (847) — Stellar accretion disks (1579)

1. INTRODUCTION

The earliest phases of star and planet formation are governed by the formation and evolution of a rotationally supported disk that mediates mass and angular momentum flow from an infalling envelope onto a newborn protostar. In the classical picture of inside-out collapse from a centrally condensed core, rotation and pressure set the conditions for disk formation and growth (Shu 1977; Terebey et al. 1984). Isothermal cores that resemble Bonnor-Ebert spheres (Bonnor 1956; Ebert 1955)

located within observable filamentary column density structures are now widely regarded as plausible initial conditions for star formation in nearby molecular clouds (André et al. 2014).

Direct observation of these embedded systems is challenging because the protostar and disk are enshrouded by a dense, optically thick envelope (Andre et al. 1993). Nevertheless, high-resolution millimeter interferometry has begun to resolve disks at the Class 0/I stages and to constrain their sizes, masses, and kinematics (Enoch et al. 2011; Tobin et al. 2012; Hara et al. 2013; Murillo et al. 2013; Codella et al. 2014; Lindberg et al. 2014; Ohashi et al. 2014, 2023; Aso et al. 2015, 2019; Maret et al. 2020). Large-sample surveys indicate that Class 0 disks are typically compact (tens of au) rather than extended, and that large ($\gtrsim 60$ au) disks are the minority (Segura-Cox et al. 2018; Maury et al. 2019; Tobin et al. 2020; Ohashi et al. 2023; Hsieh et al. 2024). These demographics, together with dust-based mass estimates,

Corresponding author: Majd Noel, Shantanu Basu
 mnoel25@uwo.ca, basu@cita.utoronto.ca

rkhann43@uwo.ca

sabbassi@uwo.ca

sami.dib@gmail.com

imply that by the Class 0/I epochs the central protostar often rivals or exceeds the disk in mass, even as inflow from the envelope continues.

Theoretical and numerical studies point to highly time-dependent accretion during the embedded phase, with elevated infall rates shortly after protostar formation and subsequent decline as the envelope is depleted (Masunaga & Inutsuka 2000; Schmeja & Klessen 2004; Dib et al. 2010). When the disk is sufficiently massive, self-gravity drives spiral arms and global asymmetries that transport angular momentum (Lin & Pringle 1987), and can trigger fragmentation and burst-mode accretion (Vorobyov & Basu 2005, 2006, 2010). In parallel, magnetic processes regulate both disk formation and angular momentum loss. In the dense, poorly ionized midplane, non-ideal magnetohydrodynamic (MHD) effects (ohmic dissipation, ambipolar diffusion, and the Hall effect) alter magnetic braking, favor disk formation, and can depend on specific field–rotation geometries (Machida et al. 2011a; Tsukamoto et al. 2015; Masson et al. 2016; Wurster & Lewis 2020; Basu et al. 2024).

Jets and wide-angle winds provide an additional channel for angular momentum extraction. Observations increasingly support a tight accretion–ejection connection in Class 0/I systems, with outflows capable of removing angular momentum from the inner envelope and disk surfaces (Pudritz & Ray 2019; Gaudel et al. 2020). In combination, gravitational torques and magnetocentrifugal winds likely set the early angular momentum budget and regulate disk growth.

Despite this progress, analytical models that jointly (i) treat envelope-fed disks in the embedded stage, (ii) include self-gravity–driven transport, and (iii) allow for mass and angular momentum loss via outflows are still limited. Many classic treatments adopt isothermal collapse or prescribe turbulent viscosity without explicit gravitational instability (GI) physics (Terebey et al. 1984; Basu 1997). A physically motivated alternative is to parameterize transport by GI itself and to seek similarity solutions for non-isothermal, self-gravitating disks (Abbassi et al. 2006, 2013). Those studies established a useful framework but employed idealized boundaries that were not explicitly tied to the thermodynamic state and mass loading of a pressure-confined parent core.

In this paper we build on that foundation and develop a self-similar, non-isothermal model for the *very early* protostellar disk (“protodisk”) immediately after protostar formation. The model couples GI-regulated angular momentum transport to an outflow torque and links the disk’s outer boundary to a pressure-confined, Bonnor–Ebert–like core through an envelope mass-infall rate. We present time-dependent solutions for the sur-

face density, temperature, specific angular momentum, and Toomre- Q , and we map the parameter space set by core sound speed, initial angular momentum content, and wind efficiency. The solutions quantify when and where the disk is gravitationally unstable, and they delineate the regimes that favor fragmentation, multiplicity, and bursty accretion.

Our scope is deliberately restricted to the nascent, self-gravity–dominated protodisk, when the stellar gravitational term and irradiation are dynamically minor. We therefore do not extrapolate these similarity solutions to typical Class 0/I systems, where surveys indicate that the star mass M_\star exceeds the disk mass M_{disk} and magnetic/irradiative effects are increasingly important (Maury et al. 2019; Tobin et al. 2020). We adopt our model for the first $\lesssim 2 \times 10^3$ yr after the protostar formation, and could be evaluated potentially till $\sim (0.5\text{--}1) \times 10^4$ yr under weak magnetic braking and strong infall; beyond this, explicit inclusion of a point-mass term and irradiation is warranted (Shu 1977; Terebey et al. 1984; Tomida et al. 2015; Tsukamoto et al. 2015; Masson et al. 2016).

In Section 2, we present the governing equations and theoretical formalism. Section 3 describes the accretion boundary condition imposed by the envelope. In Section 4, we discuss a representative solution and its time evolution. A broad parameter study is presented in Section 5, followed by an analysis of angular momentum in Section 6. In Section 7, we compare with early stage protostellar simulations, and then we conclude with a discussion of implications in Section 8.

2. MODEL

Due to the substantial angular momentum of the parental cloud core, the formation of a centrifugally-supported disk is an inevitable consequence around the newborn protostar. The equations governing the physical behavior of such accretion disks are inherently complex and challenging to solve in their full form. Therefore, we employ a self-similar approach to simplify these equations, facilitating a more tractable analysis.

Our model assumes a geometrically thin ($H/r < 1$) and axisymmetric ($\partial/\partial\phi = 0$) accretion disk around a forming protostar, where the gravitational force is dominated by the disk’s self-gravity, valid under the condition that the protostar mass $M_{\text{protostar}} \ll M_{\text{disk}}$. We intend this limit to describe the immediate post-protostar-formation, the protodisk stage, and accordingly we do not extrapolate these solutions to typical Class 0/I systems. Winds and outflows are ubiquitously observed in embedded sources (Pudritz & Ray 2019; Gaudel et al. 2020), and are a common feature in numerical simula-

tions, whether performed in local shearing boxes (Fromang et al. 2013) or in global models of core collapse (Machida & Basu 2019, 2024). These results motivate the simple wind parameterization adopted here and its inclusion alongside gravitational torques in the early envelope-fed stage.

The structural and temporal evolution of the disk is described by the vertically integrated equations of continuity, radial momentum, conservation of angular momentum, and mass loss rate:

$$\frac{\partial \sigma}{\partial t} + \frac{1}{r} \frac{\partial}{\partial r} (r \sigma v_r) + 2\dot{\sigma}_w = 0, \quad (1)$$

$$\frac{\partial v_r}{\partial t} + v_r \frac{\partial v_r}{\partial r} - \frac{j^2}{r^3} = -\frac{c_s^2}{\sigma} \frac{\partial \sigma}{\partial r} - \frac{GM_r}{r^2}, \quad (2)$$

$$\frac{\partial j}{\partial t} + v_r \frac{\partial j}{\partial r} = \frac{1}{r\sigma} \frac{\partial}{\partial r} \left[r^3 \sigma \nu \frac{\partial}{\partial r} \left(\frac{j}{r^2} \right) \right] - \frac{2j}{\sigma} (l^2 \dot{\sigma}_w), \quad (3)$$

$$\frac{\partial \dot{M}_w}{\partial r} = 4\pi r \dot{\sigma}_w, \quad (4)$$

where v_r , σ , j , ν , c_s , M_r , and \dot{M}_w represent the radial velocity, surface density, specific angular momentum, effective viscosity, sound speed, mass enclosed within a radius r , and mass-loss rate due to disk outflows, respectively. The parameter l determines the strength of the extraction for the angular momentum and

$$\dot{\sigma}_w = \rho v_z^+, \quad (5)$$

is the mass loss rate per unit area from each disk face, where v_z^+ denotes the vertical wind velocity at its base, and ρ is the mass density. The surface density is expressed by

$$\sigma = 2\rho H, \quad (6)$$

as in Abbassi et al. (2013), where

$$H = \frac{c_s^2}{2\pi G \sigma} \quad (7)$$

is the scale height of the disk. The pressure p follows a polytropic relation,

$$p = K \rho^\gamma, \quad (8)$$

where K is a constant for a given polytropic index γ .

Note that the gravitational field of a thin disk is not exactly equal to the value for a spherical distribution that is used here, but the difference is of order unity and the scaling with radius r is expected to be the same. See Appendix B for further discussion. To nondimensionalize the equations, we introduce a similarity variable (Yahil 1983; Mineshige et al. 1997):

$$x = K^{-\frac{1}{2}} G^{\frac{\gamma-1}{2}} r t^{\gamma-2}. \quad (9)$$

This transformation reduces the partial differential equations to ordinary differential equations (ODEs) in terms of the similarity variable x . As discussed in Abbassi et al. (2013), these solutions are valid under the assumptions of disk self-gravity dominance and the slow accretion limit. In line with our stated scope, gravity in Eq. (2) arises from the enclosed *disk* mass M_r only; the stellar point-mass term and irradiation are omitted because we restrict attention to the protodisk stage.

In the early stages, circumstellar disks are susceptible to GI, which can effectively transport angular momentum outward through gravitational torques (Larson 1984; Nomura & Mineshige 2000; Gammie 2001). The effective viscosity ν_{GI} due to GI is expressed as

$$\nu_{\text{GI}} = \eta \frac{G \sigma^2 r^6}{j^3} \quad (10)$$

(Lin & Pringle 1987), where η is a dimensionless parameter representing the efficiency of angular momentum transport. For an isothermal self-similar disk, Nomura & Mineshige (2000) reformulated this as $\nu'_{\text{GI}} = \eta' \Sigma^2 x^6 / J^3$, highlighting its dominance over other viscosity mechanisms in gravitationally unstable disks, where ν'_{GI} and η' are dimensionless variables in self-similar space. The variables Σ and J are dimensionless similarity variables corresponding to the surface density σ and specific angular momentum j .

After appropriate mathematical manipulations, the primary ODE describing disk evolution becomes

$$\frac{dV_r}{dx} = \frac{\frac{A}{\nu'_{\text{GI}}} + BV_r + Cx + 6 \left(\frac{V_r^2}{x} \right)}{6V_r - (3\gamma + 2)x - 4x\Gamma}, \quad (11)$$

with the coefficients

$$A = \frac{1}{x^2} [V_r - (2 - \gamma)x]^4 [V_r + (2l^2 - 1)x\Gamma], \quad (12)$$

$$B = x \frac{d\Gamma}{dx} - 3\Gamma + 12\gamma - 18, \quad (13)$$

$$C = (\gamma - 2)x \frac{d\Gamma}{dx} - 2\Gamma^2 + (5\gamma - 2)\Gamma - 10\gamma + 12. \quad (14)$$

The additional ODEs for Σ and \dot{M}_w follow similarly:

$$\frac{d\Sigma}{dx} = -\frac{\Sigma}{x} - \frac{\Sigma \left(\frac{dV_r}{dx} + \Gamma - 2\gamma + 2 \right)}{V_r + (\gamma - 2)x}, \quad (15)$$

$$\frac{d\dot{M}_w}{dx} = \Sigma x \Gamma. \quad (16)$$

These are derived in Abbassi et al. (2013). The variable \dot{M}_w is the dimensionless similarity variable of the mass loss rate \dot{M}_w , V_r is the dimensionless similarity parameter describing the radial velocity v_r , and Γ is a parameter that encapsulates the intensity of the disk winds (see

Appendix A for self-similar scaling). We numerically integrate these ODEs with respect to the similarity variable x to obtain the physical variables of interest. The boundary conditions adopted are $v_r = 0$ at the center ($x = 0$) and mass infall rate $\dot{M} = \dot{M}_{\text{infall}}$ at the outer boundary ($x = 1$), where \dot{M}_{infall} is a constant envelope infall rate during the early disk evolution (see Section 3). This setup allows us to explore the impact of envelope feeding on the disk structure and stability. For the outflow mass loss profile, we assume a power-law form: $\Lambda = \Lambda_0 x^s$ (see equation A19) where s is the scaling exponent. In the isothermal limit, Λ and Γ converge, aligning with the wind parameters described in Shadmehri (2009). Consistent with Mineshige et al. (1997), we impose a constraint on γ to ensure negative and bounded radial velocities as $x \rightarrow \infty$, adopting $\gamma = 1.1$ as our fiducial value, which lies between the isothermal ($\gamma = 1$) and adiabatic ($\gamma = 1.4$) cases. This choice is also consistent with a cool, GI-regulated protodisk in our fiducial runs.

3. PARENTAL CLOUD CORE AND ACCRETION RATES

Near-infrared observations (e.g., Alves et al. 2001; Schnee & Goodman 2005) have reported that molecular cloud cores are centrally condensed and exhibit structures that resemble Bonnor-Ebert (BE) spheres. Motivated by this, as a realistic model for the parental cloud core that begins to collapse, we consider the density profile of a critical BE sphere. The initial temperature of the isothermal core is $T = 10$ K, and the central density is $\rho_0 = 8 \times 10^{-19}$ g cm $^{-3}$, yielding a cloud radius of $R_{\text{cl}} = 0.03$ pc. Although such dense cores are considered thermally supported and gravitationally stable, they can be driven to collapse by increased external pressure or enhanced mass loading, which is consistent with recent ALMA observations of marginally stable star-forming cores in clustered environments (Chen et al. 2024). In our framework, the BE core sets the envelope mass supply to the disk during the protodisk evolutionary period modeled here.

To initiate collapse in our model, we scale the entire density profile by factors $f = 1.2, 1.68$, and 2.8 . These correspond to cloud core masses of $M_{\text{cl}} = 1.26, 2.09$, and 4.5 M $_{\odot}$, respectively. The non-enhanced BE core has a mass of approximately 0.625 M $_{\odot}$. As shown by Matsumoto & Hanawa (2003), the density enhancement factor f is related to the initial ratio of thermal to gravitational energy, α_0 , via $\alpha_0 = 0.84/f$. Thus, our f -values correspond to $\alpha_0 = 0.7, 0.5$, and 0.3 . These three cases span from marginally stable ($\alpha_0 = 0.7$) to strongly unstable ($\alpha_0 = 0.3$) parental cores, thereby bracketing the mass-loading conditions relevant to the protodisk phase.

We define three initial conditions, ρ_0 , t_{ff} and \dot{M}_{infall} that allow us to investigate how different stability states in the parent core influence disk evolution. The free-fall time is given by

$$t_{\text{ff}} = \left(\frac{3\pi}{32G\rho_0} \right)^{1/2}. \quad (17)$$

For $\rho_0 = 8 \times 10^{-19}$ g cm $^{-3}$, this yields $t_{\text{ff}} \approx 7.4 \times 10^4$ yr, which we take as the characteristic timescale that sets the envelope mass supply during the first few kyr of disk evolution.

From this, we estimate the mass infall rate as

$$\dot{M}_{\text{infall}} = \frac{M_{\text{cl}}}{t_{\text{ff}}} = \alpha_0^{-3/2} \times 10^{-5} \text{ M}_{\odot} \text{ yr}^{-1} \quad (18)$$

(see also Machida et al. 2011b). This expression shows how the infall rate scales with the degree of GI in the initial core, encapsulated by α_0 : lower α_0 (more unstable) leads to a higher \dot{M}_{infall} . Using Eq. (18), the three cases above give $\dot{M}_{\text{infall}} \approx 1.7 \times 10^{-5}, 2.8 \times 10^{-5}$, and 6.1×10^{-5} M $_{\odot}$ yr $^{-1}$, respectively. In our model, this dependence provides the key dynamical link between the thermodynamic state of the parental core and the mass loading of the forming disk; we hold \dot{M}_{infall} constant over the \sim kyr interval considered to isolate the protodisk dynamics, leaving time-variable infall to future work.

4. A FIDUCIAL CASE

Figure 1 presents the results of our fiducial model, with the parameters $\alpha_0 = 0.5$, $\eta' = 10^{-2}$, $\gamma = 1.1$, $\Lambda_0 = 0.1$, $l = 1.5$, and $s = 0.7$, illustrating the temporal evolution of disk structure at four time slices (0.5, 1, 2 and 3 kyr). For context, power-law fits are overlaid on several physical quantities to guide the eye and facilitate the interpretation. In our model, we consider the disk to be starting from $r > 5$ au, and the protostar to be $r < 5$ au, which satisfies our assumption that $M_* \ll M_{\text{disk}}$ for evolutionary timescales under review. As time progresses, the surface density in the inner region increases, while the outer region—continuously fed by infalling envelope material—shows a declining surface-density profile as the disk spreads viscously. This behavior reflects outward angular-momentum redistribution, which drives radial disk growth over kyr timescales. Adopting $K = 80$ cm $^{2.3}$ g $^{-0.1}$ s $^{-2}$, the outer radius in this fiducial solution reaches ~ 40 au at 1 kyr and ~ 70 au at 2 kyr; these values are consistent with very young Class 0 disk measurements reported in recent ALMA observations (Maureira et al. 2024). These values are shown for orientation only, since our solutions target the protodisk limit $M_{\text{disk}} \gg M_*$.

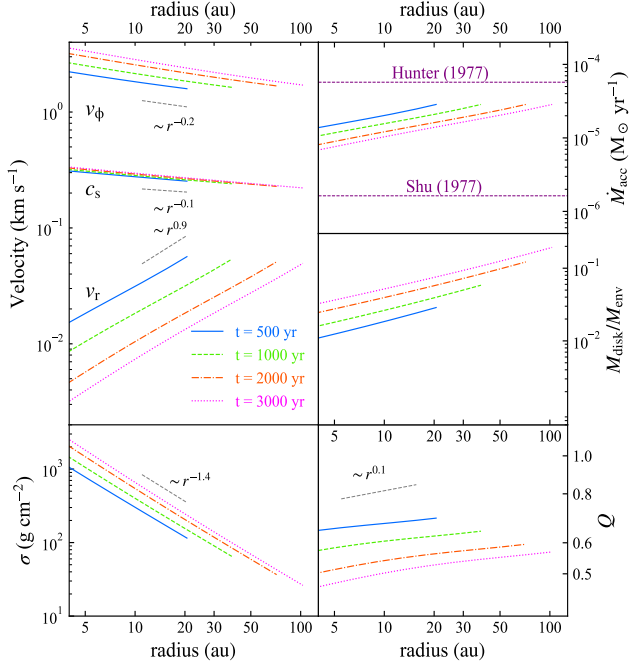


Figure 1. The profiles of the physical variables at three epochs for $\alpha_0 = 0.5$, $\eta' = 10^{-2}$, $\gamma = 1.1$ and a typical outflow emanating from the disk set at $(\Lambda_0, l, s) = (0.1, 1.5, 0.7)$. The panels show surface density, radial and tangential velocities, sound speed, and Toomre Q profiles, illustrating both the radial and temporal evolution of the system.

The gradual increase of surface density at each radius signifies a steady mass build-up in the disk+protostar system. For instance, the surface-density profile at $t = 10^3$ yr follows a power law:

$$\sigma \simeq 7.78 \times 10^3 \text{ g cm}^{-2} \left(\frac{r}{1 \text{ au}} \right)^{-1.4} \quad (19)$$

(see also Appendix B). Such normalizations and indices are observationally relevant, as they offer simplified parameterizations that can inform radiative-transfer modeling of very young disks. This agreement supports the internal consistency of our gravitational-torque-regulated model in the protodisk regime.

The tangential velocity and sound speed both increase over time in the inner regions, whereas radial velocity declines. The small ratio $|v_r|/v_\phi \ll 1$ across radii confirms the slow-accretion approximation used in the similarity reduction, and the profiles remain geometrically thin ($H/r \ll 1$). These features are consistent with self-similar viscous disk solutions (Ohtani & Tsuribe 2013).

To evaluate local gravitational stability, we adopt Toomre's Q criterion (Toomre 1964):

$$Q = \frac{c_s \kappa}{\pi G \sigma}, \quad (20)$$

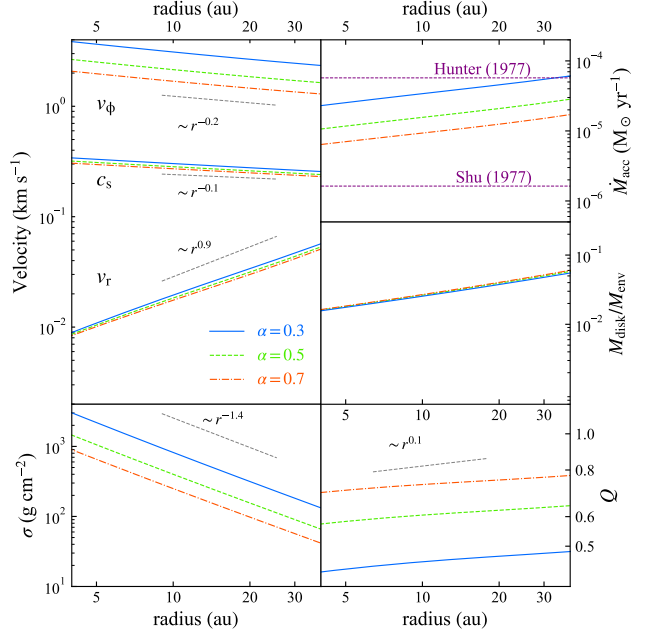


Figure 2. The profiles of the physical variables at $t = 10^3$ yr for $\alpha_0 = 0.7, 0.5, 0.3$ with $\eta = 10^{-2}$, $\gamma = 1.1$ and a typical outflow emanating from the disk set at $(\Lambda_0, l, s) = (0.1, 1.5, 0.7)$.

where

$$\kappa = \Omega \left(4 + 2 \frac{d \log \Omega}{d \log r} \right)^{1/2} \quad (21)$$

is the epicyclic frequency and $\Omega = v_\phi/r$ is the angular velocity. Values of $Q > 1$ indicate local stability against axisymmetric perturbations, whereas $Q < 1$ signals GI. In our fiducial case, the Q parameter generally decreases over time, primarily due to increasing surface density. Although the outer σ decreases slightly (which by itself would raise Q), concurrent declines in c_s and κ reduce the numerator of Q and drive a net decrease. A GI-active annulus with $Q \lesssim 1$ therefore develops and broadens with time, providing the torque that redistributes angular momentum.

The envelope infall rate governs the mass growth of the disk. Under the assumption of a constant infall rate, the mass of the disk rises with time, because the accretion of the disk towards the protostar (will be discussed further in Section 7) is less than the accretion from the envelope towards the disk. The ratio $M_{\text{disk}}/M_{\text{env}}$ (middle-right panel of Figure 1) illustrates how the disk continuously accretes material from the envelope over the first few kyr of evolution. This behavior is consistent with the results of Ohtani & Tsuribe (2013) and Machida & Hosokawa (2013), both of which support efficient disk mass growth during early accre-

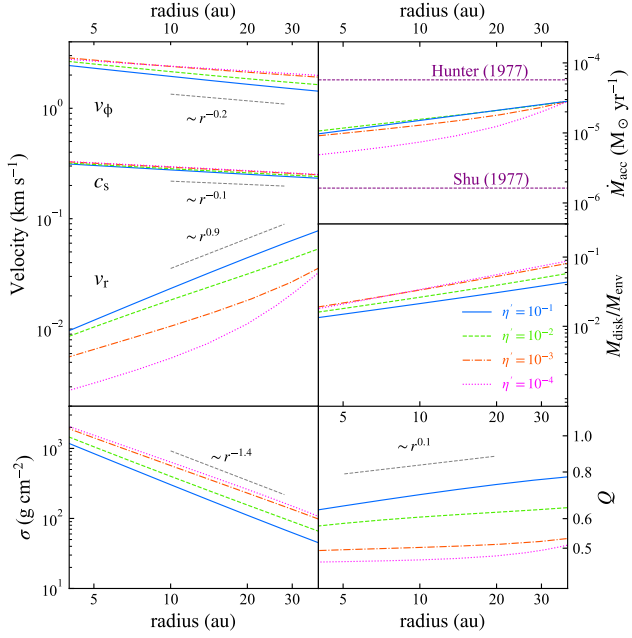


Figure 3. Same as Figure 2 but with fixed $\alpha_0 = 0.5$ and $\eta' = 10^{-1}, 10^{-2}, 10^{-3}, 10^{-4}$.

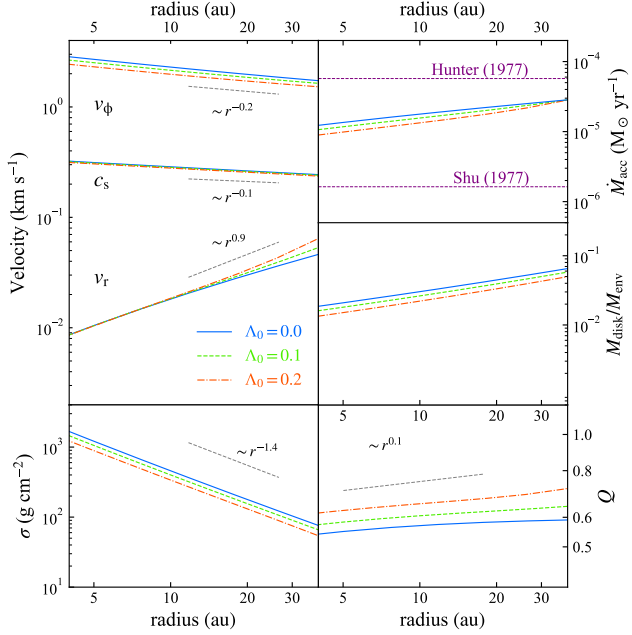


Figure 4. Same as Figure 2 but with fixed $\alpha_0 = 0.5$ and different strength attributed to outflows, i.e., $\Lambda_0 = 0, 0.1, 0.2$.

tion phases. The rapid depletion of envelope mass reported in Machida & Hosokawa (2013) further supports our model’s implication that the main accretion phase is relatively short-lived in the protodisk stage.

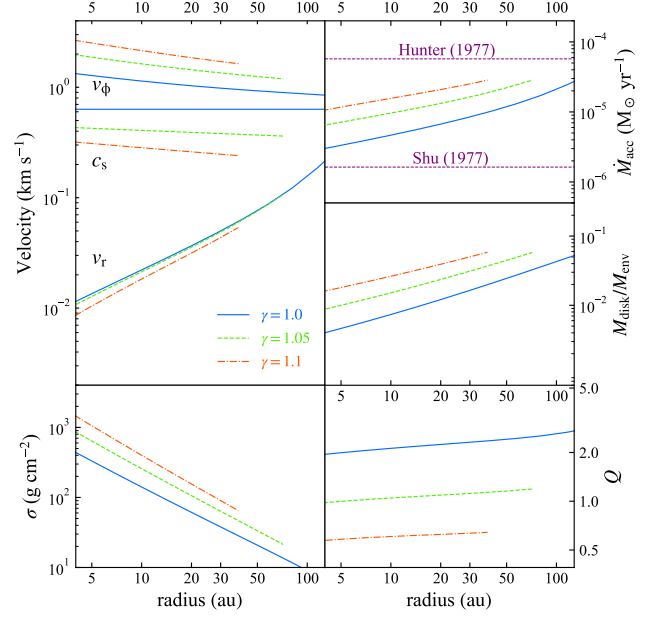


Figure 5. Same as Figure 2 but with fixed $\alpha_0 = 0.5$ and $\gamma = 1.0, 1.05, 1.1$.

Finally, it is insightful to compare our mass accretion rates with those derived from established collapse models. In general, \dot{M} scales as c_s^3/G , with the proportionality constant depending on the collapse mechanism: $\dot{M} \approx 0.975 c_s^3/G$ for inside-out collapse (Shu 1977) and $\dot{M} \approx 36 c_s^3/G$ for early collapse stages in numerical simulations (Hunter 1977). For $T = 10$ K ($c_s = 0.19$ km s $^{-1}$), these yield $\dot{M} \approx 1.6 \times 10^{-6} M_\odot$ yr $^{-1}$ and $\dot{M} \approx 5.7 \times 10^{-5} M_\odot$ yr $^{-1}$, respectively—shown in Figures 1–5 for comparison.

5. PARAMETER STUDY

In this section, we explore the influence of key parameters in our model while fixing others to their fiducial values. We assess the sensitivity of disk structure and dynamics to four primary quantities: α_0 , η' , Λ_0 , and γ —presented in Figures 2–5 for $t = 1$ kyr. An essential aim is to investigate how the physical state of the parental molecular cloud core imprints itself on the emerging disk. This is mediated by α_0 , which encodes the ratio of thermal to gravitational energy in the core and sets the disk’s outer boundary condition (see Section 2). Smaller α_0 values correspond to more massive, gravitationally unstable cores, and are the main driver of variations in \dot{M}_{infall} in our study (Machida et al. 2011b). Recent observational surveys have also emphasized that Class 0 systems with higher envelope mass tend to exhibit more massive and potentially unstable disks (Tobin et al. 2020; Maury et al. 2019). Figure 2 illustrates how

varying α_0 shapes radial profiles of disk quantities. The top-left panel reveals that lower α_0 leads to enhanced tangential velocity and sound speed. At the outer disk edge, the sound speed approaches the isothermal limit ($\sim 0.2 \text{ km s}^{-1}$), suggesting that gas becomes increasingly isothermal as it transitions from the disk to the envelope. This transition reflects the imposed boundary conditions, where the envelope was modeled with isothermal thermodynamics (see Section 3). The radial velocity exhibits only weak sensitivity to α_0 . Higher inner disk sound speed indicates elevated temperatures toward the protostar, while the velocity profile confirms faster rotation in inner layers, consistent with angular momentum transport via GI and outflows. The right-top panel shows that lower α_0 yields higher accretion rates and slightly elevated surface density (left-bottom panel). These trends follow directly from Eq. (18): smaller α_0 implies a larger \dot{M}_{infall} and hence a more rapidly mass-loaded disk.

The right-bottom panel shows a clear trend of decreasing Toomre Q with decreasing α_0 , as expected from equation (18). More unstable parental cores drive higher mass infall rates, which increase surface density and reduce Q , promoting GI (Lin & Pringle 1987). Consequently, $Q \lesssim 1$ becomes more easily satisfied in these models. The ratio $M_{\text{disk}}/M_{\text{env}}$ hardly changes due to changing α_0 , because an increase (decrease) in the mass supplied to the disk is accompanied by an increase (decrease) in mass transport in the disk due to GI. These trends are consistent with recent 3D simulations, which show that low thermal support during core collapse leads to the formation of more massive, gravitationally unstable disks (Tsukamoto et al. 2023), and that such disks can sustain GI-driven structure and fragmentation under realistic cooling conditions (Xu et al. 2025). In our similarity framework, this appears as a broadening GI-active annulus ($Q \lesssim 1$) that supplies the torque for outward angular-momentum transport.

It is informative to analyze the radial distribution of Toomre's Q . Since $Q \propto c_s \kappa / \sigma$, and the surface density σ varies more steeply with radius than the sound speed or epicyclic frequency, Q typically peaks near the outer disk where σ is lowest. Such behavior is consistent with other self-similar disk models (Shadmehri 2009; Abbassi et al. 2013), and is qualitatively similar to the isothermal collapse scenario studied by Nomura & Mineshige (2000). However, it differs from Ohtani & Tsuribe (2013), who found higher Q in the inner disk—likely due to their stiffer polytropic index ($\gamma = 1.4$) and inclusion of a central accreting protostar. In such scenarios, protostellar radiation can suppress inner disk instabilities. In contrast, our models—e.g., those shown in Figure 2—main-

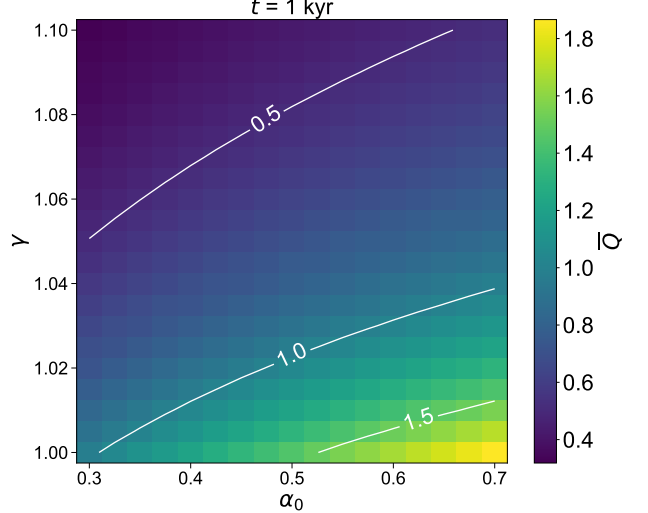


Figure 6. Grid of models with two main parameters, α_0 and γ for a snapshot of $t = 1 \text{ kyr}$. The white contours represent lines of constant \bar{Q} , which is the radially averaged Q .

tain $Q < 1$ throughout much of the disk, preserving GI and gravitational torque-driven viscosity. Recent ALMA imaging has revealed spiral structures in Class 0 disks that also point to sustained GI across large radii (Segura-Cox et al. 2020).

Figure 3 shows the impact of the effective GI viscosity parameter η' on the disk. Increasing η' —our proxy for GI efficiency—enhances angular momentum transport. This causes slight decreases in tangential velocity, sound speed, and surface density, while Q increases across the disk. Higher η' reduces the disk's capacity to retain material, thereby decreasing the accretion rate and increasing the outward radial velocity at the disk edge. Physically, larger η' corresponds to stronger spiral torques that more efficiently drain mass inward and angular momentum outward.

Figure 4 examines the effect of outflows via the wind mass-loading parameter Λ_0 . Higher Λ_0 removes more mass and angular momentum from the disk, reducing surface density and tangential velocity. Consequently, viscous dissipation decreases. Stronger outflows correlate with lower accretion rates (except at the outer edge, which is fixed), and slightly elevated radial velocities in the outer disk. The sound speed remains largely unaffected. Meanwhile, the Toomre Q value increases with Λ_0 , but remains below the GI threshold in our tested range. Thus, winds moderate disk build-up and can delay—but not entirely suppress—GI in the protodisk parameter space explored here.

The $M_{\text{disk}}/M_{\text{env}}$ ratio also declines with increasing Λ_0 , indicating that outflows eject disk mass, some of which

may be re-accreted by the envelope in realistic systems. Thus, outflows modulate disk mass accumulation efficiency. As shown in Figures 1–4, $v_\phi \propto r^{-0.2}$, which matches the theoretical profile ($r^{-0.2}$) estimated for a thin disk model in Appendix B (see Eq. B31).

In Figure 5, we test the thermodynamic sensitivity by varying γ . Raising γ from 1 to 1.1 increases surface density, tangential velocity, and accretion rate, and by that, the total disk-to-mass envelope mass ratio. In contrast, the radial velocity, sound speed, and Toomre Q all decrease. These effects reflect the stiffer pressure support in polytropic disks. Our results show that for $\gamma = 1$, the disk is gravitationally stable, while for $\gamma = 1.1$, it becomes unstable. Within our similarity framework, larger γ tends to push Q toward unity in the outer disk while leaving a broad annulus with $Q \lesssim 1$, where GI provides the dominant transport.

To map out conditions where GI remains active, we construct a grid in α_0 – γ space (Figure 6), computing the radially averaged Toomre parameter \bar{Q} . The models fall into three categories: (1) always stable ($\bar{Q} > 1$), (2) always unstable ($\bar{Q} < 1$), and (3) transitioning from stable to unstable. Our GI-based viscosity prescription is only valid in regimes where $\bar{Q} < 1$, delineating the parameter space in which our solutions are self-consistent. Accordingly, we interpret runs with $\bar{Q} \geq 1$ as diagnostic rather than predictive for transport: they indicate where a different mechanism, e.g., magnetorotational instabilities (MRI), irradiation, or a point-mass potential would need to be included. Figure 6 shows that the models generally have $\bar{Q} < 1$ within $t = 1$ kyr.

The overall result seen in Figures 1–4 is that there are notable power-laws in profiles of physical variables for models that remain nearly isothermal. Although there are small variations from model to model, we discuss the results in an average sense here. The Q parameter remains nearly spatially uniform due to the influence of the effective viscosity ν_{GI} , but there is a slightly increasing value versus radius, so we approximate $Q \propto r^{0.1}$ within the disk. The sound speed is slightly decreasing with radius and we adopt $c_s \propto r^{-0.1}$. The surface density obeys approximately $\sigma \propto r^{-1.4}$. Inserting these scalings into Eq. (20) and using Eq. (21), we find that $\Omega \propto r^{-1.2}$, therefore $v_\phi \propto r^{-0.2}$. This scaling of v_ϕ is also consistent with centrifugal balance with a gravitational field $g_{\text{disk}} \propto r^{-1.4}$ that emerges naturally from a surface density $\sigma \propto r^{-1.4}$. See Appendix B for details.

Uncertainties in observationally inferred disk masses remain significant due to systematic dependencies on dust opacities, temperature assumptions, and simplified radiative transfer models. We revisit these limitations and their implications in Section 8. Overall, the param-

eter trends here identify a self-consistent window—set by α_0 , η' , Λ_0 , and γ —in which GI and winds regulate the early protodisk before the epoch when the stellar potential and irradiation must be included explicitly.

6. ANGULAR MOMENTUM EVOLUTION

Angular momentum is transported from the faster inner disk to the slower outer regions via gravitational torques and disk winds. In the earliest phase, the angular momentum inherited from the collapsing core is transferred to the disk. We analyze the evolution of the specific angular momentum in the disk, where the total angular momentum is

$$J_{\text{disk}} = \int r v_\phi(r) \sigma(r) 2\pi r \, dr, \quad (22)$$

and the mass-weighted specific angular momentum is $J_M \equiv J_{\text{disk}}/M_{\text{disk}}$.

The left panel of Figure 7 shows the time evolution of the specific angular momentum for different values of α_0 and Λ_0 (outflows and no outflows cases), with other parameters fixed at their fiducial values. As the disk grows in mass and size, its specific angular momentum increases over time. This is the expected scaling in a self-gravitating disk, as both the enclosed disk mass and characteristic radius increase, the mass-weighted J_M rises because the outer disk stores the angular momentum transported from inner radii. This behavior is consistent with results from previous numerical simulations (Hayfield et al. 2011; Joos et al. 2012) and reflects the buildup of angular momentum from sustained envelope accretion.

The presence of outflows leads to a measurable reduction in specific angular momentum over time, as shown by the difference between dashed and solid curves in the left panel of Figure 7. Physically, winds remove high-specific-angular-momentum material from the disk surface and carry an extra torque through the magnetic lever arm (parameter l in our model), thereby reducing J_M even when mass loss is modest. This supports the interpretation that disk winds act as a secondary angular momentum loss channel, particularly relevant in the early phases (Lebreuilly et al. 2024).

The right panel of Figure 7 explores how J_M varies with η' and α_0 . Increasing η' reduces the specific angular momentum J_M , as stronger gravitational torques enhance outward transport of the angular momentum. Lowering α_0 increases the envelope mass-loading (Eq. 18), which boosts J_M at fixed time by growing the disk and shifting more angular momentum to larger radii. These trends are again in line with theoretical expectations for GI-regulated disks (Lin & Pringle 1987; Kratter et al. 2010).

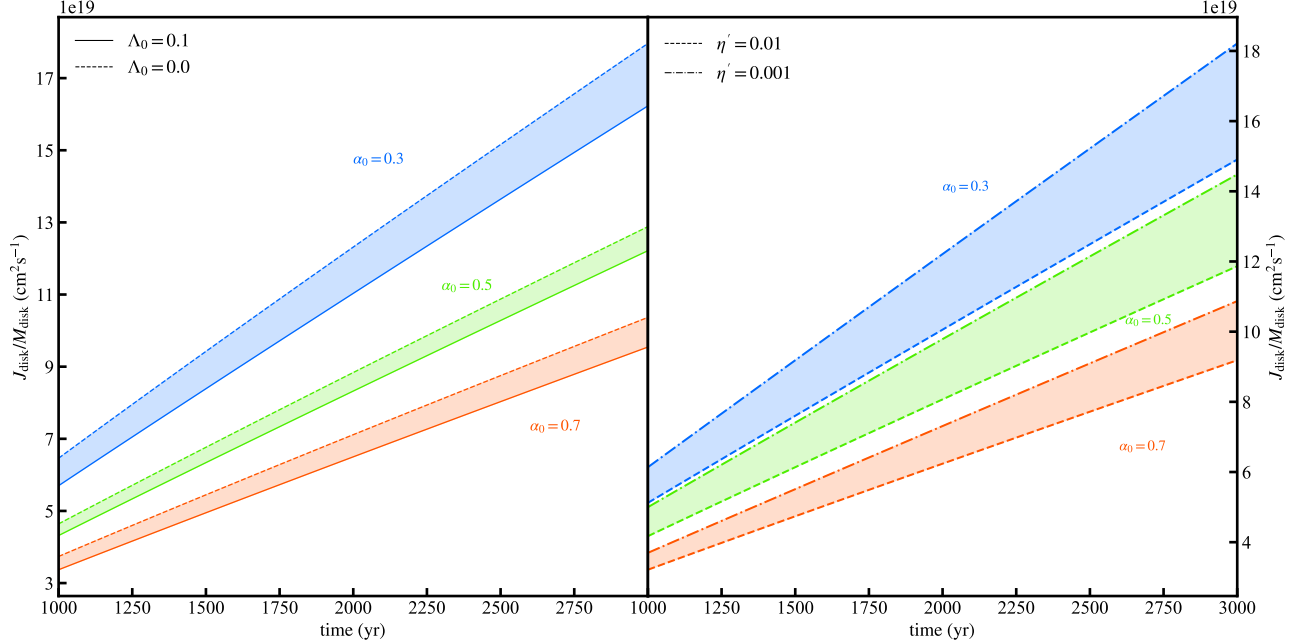


Figure 7. Left: Time evolution of the specific angular momentum (units: $10^{19} \text{ cm}^2 \text{ s}^{-1}$) of the circumstellar disk, for different α_0 and Λ_0 , up to 3 kyr after the onset of protostar formation. Dashed lines correspond to solutions without any outflow. Right: Time evolution of the specific angular momentum of the circumstellar disk, for different α_0 and η' .

Measurements on cloud scales typically yield specific angular momenta around $\sim 10^{21} - 10^{22} \text{ cm}^2 \text{ s}^{-1}$ (Goodman et al. 1993), greater than those of individual disks. Figure 8 provides a schematic of J_{M} values across spatial scales and evolutionary stages. Our models offer a self-consistent explanation for the several-orders-of-magnitude angular momentum reduction required during collapse and disk formation—a core challenge known as the “angular momentum problem” in star formation theory (Spitzer 1978). In our picture, the protodisk absorbs the angular momentum of the core, GI torques redistribute it radially, and the winds remove a fraction, setting the initial conditions for later star-dominated evolution. The GI torques in our model lead to angular momentum redistribution and mass accretion in a smoothly varying manner that can be considered to be the time average of a process that will more realistically also include episodic bursts (Vorobyov & Basu 2005, 2006, 2010).

This behavior is also consistent with recent disk formation simulations (e.g., Tsukamoto et al. 2023) that show that the early circumstellar disk acts as a reservoir absorbing angular momentum from the collapsing core. After the second collapse phase, the residual disk continues to accrete angular momentum and expands outward. We therefore interpret the increase of J_{M} with time as a robust feature of the protodisk stage; beyond this stage, once $M_{\star} \gtrsim M_{\text{disk}}$ and irradiation becomes im-

portant, a different angular-momentum budget should be considered.

7. COMPARISON WITH MAGNETIC AND HYDRODYNAMIC MODELS

We explore the disk’s temporal evolution until $t = 2000$ yr, by alternating both the outflow efficiency governed by the wind loading parameter Λ_0 and the angular momentum transport parameter η' . In Figure 9, the left panels show physical quantities for a snapshot of the disk at $t = 1000$ yr and compare how different combinations of Λ_0 and η' affect the rotational motion, accretion, and stability of the disk. We assume the protostar accretion would dominate the inner accretion within ($r < 5$ au). Therefore, the right panels show the protostellar accretion rate \dot{M}_{\star} (measured at $r = 5$ au) and the ratio of protostellar accretion (\dot{M}_{\star}) to protodisk accretion (\dot{M}_{acc}).

The properties, including tangential velocity, disk mass, protostellar and protodisk accretion rate, obtained by our self-similar model are in a similar range as Machida et al. (2010), involving purely hydrodynamical simulations in the first 10^4 yr after the protostar formation, when $M_{\text{disk}} \gg M_{\star}$. They differ slightly from Machida et al. (2011a) and Machida & Basu (2019) due to the influence of magnetic fields that initiate magnetic braking and outflows. Because of the presence of magnetic fields in their models, the disk does not grow in size until the magnetic fields are diffused significantly.

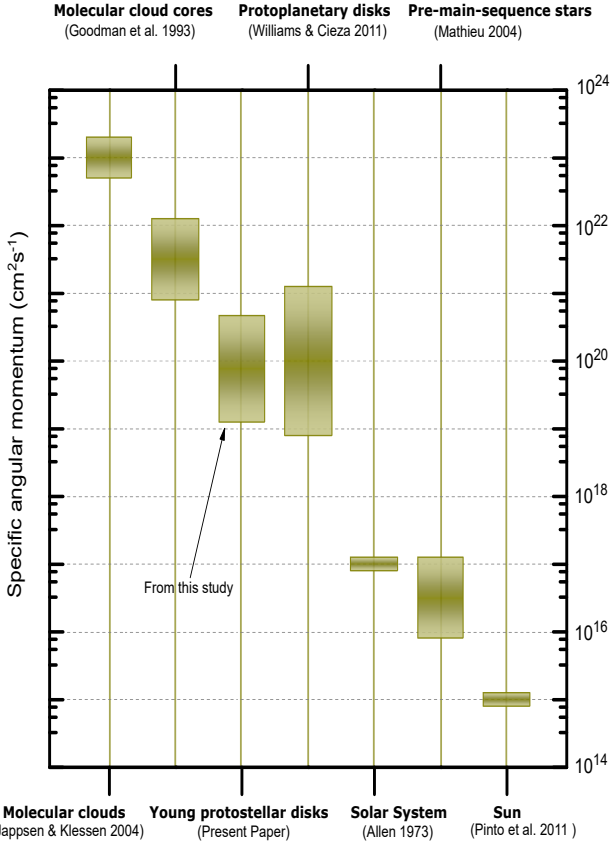


Figure 8. Schematic representation of typical specific angular momenta over different scales and stages in stellar evolution, from molecular clouds (Goodman et al. 1993; Jappsen & Klessen 2004), to protoplanetary disks (Williams & Cieza 2011), and finally to pre-main-sequence stars and the Sun (Allen 1973; Mathieu 2004; Pinto et al. 2011)

However, we observe that changing Λ_0 and η' leads to efficient mass outflow and angular momentum transport from the inner regions, bringing us closer to the early stage disk properties seen in MHD simulations.

Small values for η' and Λ_0 lead to ineffective angular momentum transport and weak outflows, respectively. This results in more mass and angular momentum retained within the inner regions of the disk. Therefore, the Toomre parameter Q remains sufficiently within the unstable range even near the outer disk's boundary. This is recorded in the simulations of Machida et al. (2010). In their simulations, the absence of magnetic fields results in no magnetic braking and weak outflows. This leads to a steady increase in the disk's mass and size. The disk maintains average Toomre Q lower than unity until the protostar grows in size and becomes comparable to the disk in mass.

In Figure 9, we plot physical parameters that have been extensively studied in early-stage protostellar-disk simulations (Machida et al. 2010, 2011a; Machida & Basu 2019). We plot the ratio of the radial velocity v_r to the tangential velocity v_ϕ in the upper left panel. The ratio is always greater than unity. This is because of the slow accretion limit assumption in our model. The steady increase in the ratio of radial to tangential velocity is explained by the observations made in Figure 3 and Figure 4. Increasing the GI viscosity parameter η' leads to higher accretion, and increasing the outflow parameter Λ_0 transports angular momentum of the protodisk to outer regions, causing the outer regions of the disk to have higher radial velocities. Higher Λ_0 and η' lead to a complex interplay of physical effects. Higher Λ_0 continuously transfer mass and angular momentum out of the system through stronger winds, and the disk loses mass and becomes less prone to gravitational instabilities. However, higher η' induce gravitational instabilities and maintain efficient angular momentum transport, which causes gravitational torques to transfer mass into the inner regions of the disk. Because of the interplay between higher Λ_0 and η' , no significant influence is seen in the inner accretion of the disk, resulting in a relatively unchanged protostellar accretion rate.

Machida & Basu (2019) simulated a collapsing core where magnetic fields slowly dissipate, causing angular momentum to be less effectively transferred and for outflows to decay. The disk surface density in their model gradually increases and causes GI and accompanying gravitational torques to operate. This is consistent with our model, where weaker outflows and higher surface density result in a disk more prone to GI. The protodisk mass remains greater than the protostellar mass, which is observed in the unmagnetized core collapse simulations performed by Machida et al. (2010).

In the lower left panel, we can see that increasing the outflow parameter and viscosity leads the system to greater stability and higher Q values. This is because viscosity increases the angular momentum transport, which leads to the system losing mass. Since the induced GI viscosity depends on the disk mass, this will make the system more stable and lead to the Toomre parameter Q being closer to stability.

In the upper right panel, we compare our results of protostellar accretion rates with that of Machida & Basu (2019), finding the values to be in a similar range. Although the model does not include a protostar, in the sense that the mass of the protostar is negligible ($M_* \ll M_{\text{disk}}$), and does not contribute to the gravitational potential, the accretion from the disk to an inner region still happens. In the lower right panel, the ratio

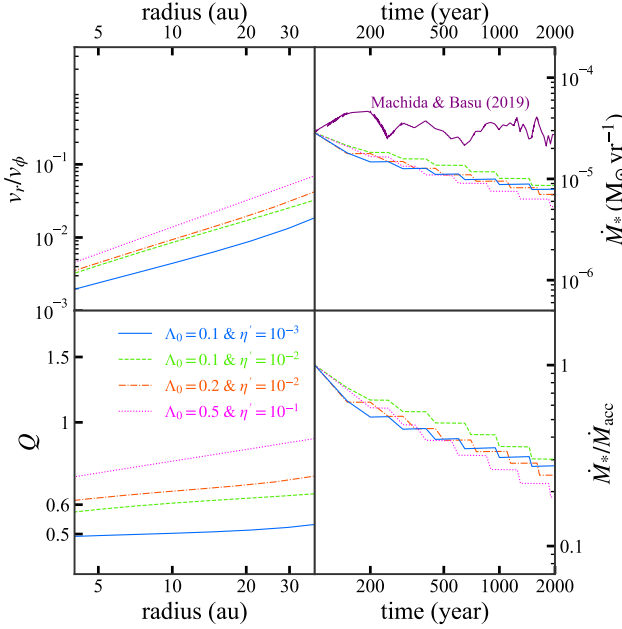


Figure 9. Ratio of radial v_r to tangential velocity v_ϕ along with the Toomre Q as a function of radius at $t = 1000$ yr. The protostellar mass accretion rate \dot{M}_* and the ratio of protostellar to disk accretion rates $\dot{M}_*/\dot{M}_{\text{acc}}$ are plotted for the first 2000 yr of protostellar evolution. The mass accretion rate from the simulation of Machida & Basu (2019) is shown for comparison.

of the protostar's mass accretion to the disk accretion is plotted. The accretion from the envelope to the disk is greater than the accretion from the disk to the protostar, and the ratio is always less than unity after a couple of hundred years of evolution, making it consistent with our model's assumptions.

8. CONCLUSIONS

We investigated the structure and early dynamical evolution of the immediate post-protostar-formation, self-gravity-dominated protodisk (i.e., $M_{\text{disk}} \gg M_*$). Our model neglects the gravitational force of the central protostar by restricting the analysis to the first few kyr of disk evolution, during which the disk mass dominates. In practice, we treat the stellar point-mass term and irradiation as dynamically minor and omit them from the equations; we therefore do not extrapolate our solutions to typical Class 0/I systems where $M_* \gtrsim M_{\text{disk}}$. We adopted a polytropic pressure-density relation and parameterized angular momentum loss via disk outflows. Gravitational instability (GI) was modeled through the effective viscosity prescription of Lin & Pringle (1987). A rough applicability window is the first $\lesssim 2 \times 10^3$ yr after protostar formation.

A central theme of this work is the link between the initial conditions of the molecular cloud core and the resulting disk properties. We introduced the parameter α_0 to control the mass infall rate from the envelope to the disk and studied its effect alongside three other critical parameters: the polytropic index γ , the wind strength parameter Λ_0 , and the efficiency of GI-induced angular momentum transport η' . This mapping from $(\alpha_0, \gamma, \Lambda_0, \eta')$ to disk structure provides an analytic, self-similar framework for identifying where GI and winds regulate the protodisk.

Our theoretical model predicts relatively high disk-to-envelope mass ratios, particularly for low α_0 cases that represent more gravitationally unstable parental cores. At first glance, these values may appear higher than those inferred from dust continuum observations of Class 0 protostars. However, this discrepancy may be due to systematic biases in observational mass estimates. Tsukamoto et al. (2017) demonstrated through radiation hydrodynamic simulations that in gravitationally unstable disks, dust growth and depletion of small grains can significantly lower the millimeter-wave opacity. This leads to an underestimation of the disk mass by a factor of 3 to 5 when standard interstellar medium dust properties are assumed. Given that our regime targets GI-active, rapidly evolving protodisks, such opacity effects could naturally move observed M_{disk} estimates toward our predicted values.

Comparisons with early-stage protostellar-disk simulations provided insight into the applicability of our theoretical model. In our theoretical model the disk evolves with properties resembling hydrodynamical simulations in the first 10^3 to 10^4 yr because we did not consider magnetic fields in the self-similar model. Adjusting the key parameters, specifically Λ_0 and η' , induces efficient angular momentum transport to the outer-regions due to GI viscosity and stronger wind efficiencies, resulting in the protodisk having properties similar to those observed in MHD simulations.

Due to the inherent limitations of similarity solutions near boundaries, we did not model the detailed transition from disk to protostar. In our formulation, the disk mass includes the mass that will eventually accrete onto the central object. Likewise, fragmentation physics and radiative feedback are beyond the present scope and are deferred to future work. Our theoretical analysis highlights several key trends:

- Disks originating from more gravitationally unstable cores (lower α_0) rotate more rapidly, exhibit higher accretion rates, and develop systematically higher surface densities. Such disks are more prone to GI, as indicated by lower Toomre Q values.

- While gravitational torques and disk outflows act to extract angular momentum, continued envelope accretion replenishes it. This results in a net monotonic increase in specific angular momentum throughout the early disk evolution.
- Increased efficiency of angular momentum transport (i.e., higher values of η') leads to more effective outward transfer of angular momentum, thereby reducing the amount retained within the disk.
- The centrifugally supported disk is characterized by a profile shallower than Keplerian in which we find the approximate relation $v_\phi \propto r^{-0.2}$. This follows from a surface density σ and resulting gravitational field g_{disk} that both scale as $\propto r^{-1.4}$.

Together, these results underscore the importance of GI and envelope feeding in governing the dynamical evolution of protostellar disks. Outflows and internal GI torques lead to a significant loss of angular momentum that works toward resolving the angular momentum problem of star formation. Our model suggests that the structure, stability, and mass content of the protodisk are primarily determined by the thermodynamic state of the parental core and the efficiency of GI and winds; beyond this stage, as M_* grows and the irradiation strengthens, a different (star-dominated) framework must be applied.

S. B. is supported by a Discovery Grant from the Natural Sciences and Engineering Council of Canada.

REFERENCES

Abbassi, S., Ghanbari, J., & Salehi, F. 2006, A&A, 460, 357, doi: [10.1051/0004-6361:20064805](https://doi.org/10.1051/0004-6361:20064805)

Abbassi, S., Nourbakhsh, E., & Shadmehri, M. 2013, ApJ, 765, 96, doi: [10.1088/0004-637X/765/2/96](https://doi.org/10.1088/0004-637X/765/2/96)

Allen, C. W. 1973, *Astrophysical quantities*

Alves, J. F., Lada, C. J., & Lada, E. A. 2001, Nature, 409, 159, doi: [10.1038/35051509](https://doi.org/10.1038/35051509)

André, P., Di Francesco, J., Ward-Thompson, D., et al. 2014, in *Protostars and Planets VI*, ed. H. Beuther, R. S. Klessen, C. P. Dullemond, & T. Henning, 27–51, doi: [10.2458/azu_uapress_9780816531240-ch002](https://doi.org/10.2458/azu_uapress_9780816531240-ch002)

Andre, P., Ward-Thompson, D., & Barsony, M. 1993, ApJ, 406, 122, doi: [10.1086/172425](https://doi.org/10.1086/172425)

Aso, Y., Ohashi, N., Saigo, K., et al. 2015, ApJ, 812, 27, doi: [10.1088/0004-637X/812/1/27](https://doi.org/10.1088/0004-637X/812/1/27)

Aso, Y., Hirano, N., Aikawa, Y., et al. 2019, ApJ, 887, 209, doi: [10.3847/1538-4357/ab5284](https://doi.org/10.3847/1538-4357/ab5284)

Basu, S. 1997, ApJ, 485, 240, doi: [10.1086/304420](https://doi.org/10.1086/304420)

Basu, S., & Mouschovias, T. C. 1994, ApJ, 432, 720, doi: [10.1086/174611](https://doi.org/10.1086/174611)

Basu, S., Sharkawi, M., & Machida, M. N. 2024, ApJ, 964, 116, doi: [10.3847/1538-4357/ad1bf3](https://doi.org/10.3847/1538-4357/ad1bf3)

Bonnor, W. B. 1956, MNRAS, 116, 351, doi: [10.1093/mnras/116.3.351](https://doi.org/10.1093/mnras/116.3.351)

Chen, C.-Y., Friesen, R., Li, J., et al. 2024, MNRAS, 527, 10279, doi: [10.1093/mnras/stad3868](https://doi.org/10.1093/mnras/stad3868)

Codella, C., Cabrit, S., Gueth, F., et al. 2014, A&A, 568, L5, doi: [10.1051/0004-6361/201424103](https://doi.org/10.1051/0004-6361/201424103)

Dib, S., Shadmehri, M., Padoan, P., et al. 2010, MNRAS, 405, 401, doi: [10.1111/j.1365-2966.2010.16451.x](https://doi.org/10.1111/j.1365-2966.2010.16451.x)

Ebert, R. 1955, ZA, 37, 217

Enoch, M. L., Corder, S., Duchêne, G., et al. 2011, ApJS, 195, 21, doi: [10.1088/0067-0049/195/2/21](https://doi.org/10.1088/0067-0049/195/2/21)

Fromang, S., Latter, H., Lesur, G., & Ogilvie, G. I. 2013, A&A, 552, A71, doi: [10.1051/0004-6361/201220016](https://doi.org/10.1051/0004-6361/201220016)

Gammie, C. F. 2001, ApJ, 553, 174, doi: [10.1086/320631](https://doi.org/10.1086/320631)

Gaudel, M., Maury, A. J., Belloche, A., et al. 2020, A&A, 637, A92, doi: [10.1051/0004-6361/201936364](https://doi.org/10.1051/0004-6361/201936364)

Goodman, A. A., Benson, P. J., Fuller, G. A., & Myers, P. C. 1993, ApJ, 406, 528, doi: [10.1086/172465](https://doi.org/10.1086/172465)

Hara, C., Shimajiri, Y., Tsukagoshi, T., et al. 2013, ApJ, 771, 128, doi: [10.1088/0004-637X/771/2/128](https://doi.org/10.1088/0004-637X/771/2/128)

Hayfield, T., Mayer, L., Wadsley, J., & Boley, A. C. 2011, MNRAS, 417, 1839, doi: [10.1111/j.1365-2966.2011.19371.x](https://doi.org/10.1111/j.1365-2966.2011.19371.x)

Hsieh, C.-H., Arce, H. G., Maureira, M. J., et al. 2024, ApJ, 973, 138, doi: [10.3847/1538-4357/ad152](https://doi.org/10.3847/1538-4357/ad152)

Hunter, C. 1977, ApJ, 218, 834, doi: [10.1086/155739](https://doi.org/10.1086/155739)

Jappsen, A.-K., & Klessen, R. S. 2004, A&A, 423, 1, doi: [10.1051/0004-6361:20040220](https://doi.org/10.1051/0004-6361:20040220)

Joos, M., Hennebelle, P., & Ciardi, A. 2012, A&A, 543, A128, doi: [10.1051/0004-6361/201118730](https://doi.org/10.1051/0004-6361/201118730)

Kratter, K. M., Matzner, C. D., Krumholz, M. R., & Klein, R. I. 2010, ApJ, 708, 1585, doi: [10.1088/0004-637X/708/2/1585](https://doi.org/10.1088/0004-637X/708/2/1585)

Larson, R. B. 1984, MNRAS, 206, 197, doi: [10.1093/mnras/206.1.197](https://doi.org/10.1093/mnras/206.1.197)

Lebreuilly, U., Hennebelle, P., Maury, A., et al. 2024, A&A, 683, A13, doi: [10.1051/0004-6361/202347913](https://doi.org/10.1051/0004-6361/202347913)

Lin, D. N. C., & Pringle, J. E. 1987, Monthly Notices of the Royal Astronomical Society, 225, 607, doi: [10.1093/mnras/225.3.607](https://doi.org/10.1093/mnras/225.3.607)

Lindberg, J. E., Jørgensen, J. K., Brinch, C., et al. 2014, *A&A*, 566, A74, doi: [10.1051/0004-6361/201322651](https://doi.org/10.1051/0004-6361/201322651)

Machida, M. N., & Basu, S. 2019, *ApJ*, 876, 149, doi: [10.3847/1538-4357/ab18a7](https://doi.org/10.3847/1538-4357/ab18a7)

—. 2024, *ApJ*, 970, 41, doi: [10.3847/1538-4357/ad4997](https://doi.org/10.3847/1538-4357/ad4997)

Machida, M. N., & Hosokawa, T. 2013, *MNRAS*, 431, 1719, doi: [10.1093/mnras/stt291](https://doi.org/10.1093/mnras/stt291)

Machida, M. N., Inutsuka, S.-i., & Matsumoto, T. 2010, *ApJ*, 724, 1006, doi: [10.1088/0004-637X/724/2/1006](https://doi.org/10.1088/0004-637X/724/2/1006)

—. 2011a, *PASJ*, 63, 555, doi: [10.1093/pasj/63.3.555](https://doi.org/10.1093/pasj/63.3.555)

—. 2011b, *ApJ*, 729, 42, doi: [10.1088/0004-637X/729/1/42](https://doi.org/10.1088/0004-637X/729/1/42)

Maret, S., Maury, A. J., Belloche, A., et al. 2020, *A&A*, 635, A15, doi: [10.1051/0004-6361/201936798](https://doi.org/10.1051/0004-6361/201936798)

Masson, J., Chabrier, G., Hennebelle, P., Vaytet, N., & Commerçon, B. 2016, *A&A*, 587, A32, doi: [10.1051/0004-6361/201526371](https://doi.org/10.1051/0004-6361/201526371)

Masunaga, H., & Inutsuka, S.-i. 2000, *ApJ*, 531, 350, doi: [10.1086/308439](https://doi.org/10.1086/308439)

Mathieu, R. D. 2004, in *IAU Symposium*, Vol. 215, Stellar Rotation, ed. A. Maeder & P. Eenens, 113

Matsumoto, T., & Hanawa, T. 2003, *ApJ*, 595, 913, doi: [10.1086/377367](https://doi.org/10.1086/377367)

Maureira, M. J., Pineda, J. E., Liu, H. B., et al. 2024, *A&A*, 689, L5, doi: [10.1051/0004-6361/202451166](https://doi.org/10.1051/0004-6361/202451166)

Maury, A. J., André, P., Testi, L., et al. 2019, *A&A*, 621, A76, doi: [10.1051/0004-6361/201833537](https://doi.org/10.1051/0004-6361/201833537)

Mineshige, S., Nakayama, K., & Umemura, M. 1997, *PASJ*, 49, 439, doi: [10.1093/pasj/49.4.439](https://doi.org/10.1093/pasj/49.4.439)

Morton, S. A., Mouschovias, T. C., & Ciolek, G. E. 1994, *ApJ*, 421, 561, doi: [10.1086/173671](https://doi.org/10.1086/173671)

Murillo, N. M., Lai, S.-P., Bruderer, S., Harsono, D., & van Dishoeck, E. F. 2013, *A&A*, 560, A103, doi: [10.1051/0004-6361/201322537](https://doi.org/10.1051/0004-6361/201322537)

Nomura, H., & Mineshige, S. 2000, *ApJ*, 536, 429, doi: [10.1086/308919](https://doi.org/10.1086/308919)

Ohashi, N., Saigo, K., Aso, Y., et al. 2014, *ApJ*, 796, 131, doi: [10.1088/0004-637X/796/2/131](https://doi.org/10.1088/0004-637X/796/2/131)

Ohashi, N., Tobin, J. J., Jørgensen, J. K., et al. 2023, *ApJ*, 951, 8, doi: [10.3847/1538-4357/acd384](https://doi.org/10.3847/1538-4357/acd384)

Ohtani, T., & Tsuribe, T. 2013, *PASJ*, 65, 93, doi: [10.1093/pasj/65.4.93](https://doi.org/10.1093/pasj/65.4.93)

Pinto, R. F., Brun, A. S., Jouve, L., & Grappin, R. 2011, *ApJ*, 737, 72, doi: [10.1088/0004-637X/737/2/72](https://doi.org/10.1088/0004-637X/737/2/72)

Pudritz, R. E., & Ray, T. P. 2019, *Frontiers in Astronomy and Space Sciences*, 6, 54, doi: [10.3389/fspas.2019.00054](https://doi.org/10.3389/fspas.2019.00054)

Schmeja, S., & Klessen, R. S. 2004, *A&A*, 419, 405, doi: [10.1051/0004-6361:20034375](https://doi.org/10.1051/0004-6361:20034375)

Schnee, S., & Goodman, A. 2005, *ApJ*, 624, 254, doi: [10.1086/429156](https://doi.org/10.1086/429156)

Segura-Cox, D. M., Looney, L. W., Tobin, J. J., et al. 2018, *ApJ*, 866, 161, doi: [10.3847/1538-4357/aaddf3](https://doi.org/10.3847/1538-4357/aaddf3)

Segura-Cox, D. M., Schmiedeke, A., Pineda, J. E., et al. 2020, *Nature*, 586, 228, doi: [10.1038/s41586-020-2779-6](https://doi.org/10.1038/s41586-020-2779-6)

Shadmehri, M. 2009, *MNRAS*, 395, 877, doi: [10.1111/j.1365-2966.2009.14561.x](https://doi.org/10.1111/j.1365-2966.2009.14561.x)

Shu, F. H. 1977, *The Astrophysical Journal*, 214, 488, doi: [10.1086/155274](https://doi.org/10.1086/155274)

Spitzer, L. 1978, *Physical processes in the interstellar medium*, doi: [10.1002/9783527617722](https://doi.org/10.1002/9783527617722)

Terebey, S., Shu, F. H., & Cassen, P. 1984, *The Astrophysical Journal*, 286, 529, doi: [10.1086/162628](https://doi.org/10.1086/162628)

Tobin, J. J., Hartmann, L., Chiang, H.-F., et al. 2012, *Nature*, 492, 83, doi: [10.1038/nature11610](https://doi.org/10.1038/nature11610)

Tobin, J. J., Sheehan, P. D., Megeath, S. T., et al. 2020, *ApJ*, 890, 130, doi: [10.3847/1538-4357/ab6f64](https://doi.org/10.3847/1538-4357/ab6f64)

Tomida, K., Okuzumi, S., & Machida, M. N. 2015, *ApJ*, 801, 117, doi: [10.1088/0004-637X/801/2/117](https://doi.org/10.1088/0004-637X/801/2/117)

Toomre, A. 1963, *ApJ*, 138, 385, doi: [10.1086/147653](https://doi.org/10.1086/147653)

—. 1964, *ApJ*, 139, 1217, doi: [10.1086/147861](https://doi.org/10.1086/147861)

Tsukamoto, Y., Iwasaki, K., Okuzumi, S., Machida, M. N., & Inutsuka, S. 2015, *MNRAS*, 452, 278, doi: [10.1093/mnras/stv1290](https://doi.org/10.1093/mnras/stv1290)

Tsukamoto, Y., Machida, M. N., & Inutsuka, S.-i. 2023, *PASJ*, 75, 835, doi: [10.1093/pasj/psad040](https://doi.org/10.1093/pasj/psad040)

Tsukamoto, Y., Okuzumi, S., & Kataoka, A. 2017, *ApJ*, 838, 151, doi: [10.3847/1538-4357/aa6081](https://doi.org/10.3847/1538-4357/aa6081)

Vorobyov, E. I., & Basu, S. 2005, *ApJL*, 633, L137, doi: [10.1086/498303](https://doi.org/10.1086/498303)

—. 2006, *ApJ*, 650, 956, doi: [10.1086/507320](https://doi.org/10.1086/507320)

—. 2010, *ApJ*, 719, 1896, doi: [10.1088/0004-637X/719/2/1896](https://doi.org/10.1088/0004-637X/719/2/1896)

Williams, J. P., & Cieza, L. A. 2011, *ARA&A*, 49, 67, doi: [10.1146/annurev-astro-081710-102548](https://doi.org/10.1146/annurev-astro-081710-102548)

Wurster, J., & Lewis, B. T. 2020, *MNRAS*, 495, 3795, doi: [10.1093/mnras/staa1339](https://doi.org/10.1093/mnras/staa1339)

Xu, W., Jiang, Y.-F., Kunz, M. W., & Stone, J. M. 2025, *ApJ*, 986, 91, doi: [10.3847/1538-4357/add14a](https://doi.org/10.3847/1538-4357/add14a)

Yahil, A. 1983, *ApJ*, 265, 1047, doi: [10.1086/160746](https://doi.org/10.1086/160746)

APPENDIX

A. SIMILARITY TRANSFORMATION

The following dimensionless similarity variables describe the time-dependent evolution of the physical quantities in our model.

Surface density:

$$\sigma(r, t) = (2\pi)^{-1} K^{1/2} G^{-(1+\gamma)/2} t^{-\gamma} \Sigma(x). \quad (\text{A1})$$

Volume density:

$$\rho(r, t) = (4\pi\gamma)^{-1/\gamma} G^{-1} t^{-2} \Sigma^{2/\gamma}(x). \quad (\text{A2})$$

Pressure:

$$p(r, t) = (4\pi\gamma)^{-1} K G^{-\gamma} t^{-2\gamma} \Sigma^2(x). \quad (\text{A3})$$

Sound speed:

$$c_s(r, t) = (4\pi)^{(1-\gamma)/(2\gamma)} \gamma^{1/(2\gamma)} K^{1/2} G^{(1-\gamma)/2} t^{1-\gamma} \Sigma^{(\gamma-1)/\gamma}(x). \quad (\text{A4})$$

Radial velocity:

$$v_r(r, t) = K^{1/2} G^{(1-\gamma)/2} t^{1-\gamma} V_r(x). \quad (\text{A5})$$

Tangential velocity:

$$v_\phi(r, t) = K^{1/2} G^{(1-\gamma)/2} t^{1-\gamma} V_\phi(x). \quad (\text{A6})$$

Vertical velocity from outflows:

$$v_z^+(r, t) = K^{1/2} G^{(1-\gamma)/2} t^{1-\gamma} V_z^+(x). \quad (\text{A7})$$

Specific angular momentum:

$$j(r, t) = K G^{1-\gamma} t^{3-2\gamma} J(x). \quad (\text{A8})$$

Vertical scale height:

$$H(r, t) = (4\pi)^{(1-\gamma)/\gamma} \gamma^{1/\gamma} K^{1/2} G^{(1-\gamma)/2} t^{2-\gamma} \Sigma^{(\gamma-2)/\gamma}(x). \quad (\text{A9})$$

Effective viscosity:

$$\nu(r, t) = K G^{1-\gamma} t^{3-2\gamma} \nu'(x). \quad (\text{A10})$$

Cumulative mass interior to radius r :

$$M_r(r, t) = K^{3/2} G^{(1-3\gamma)/2} t^{4-3\gamma} \mathcal{M}_x(x). \quad (\text{A11})$$

Mass accretion rate:

$$\dot{M}_{\text{acc}}(r, t) = -2\pi r \sigma v_r = K^{3/2} G^{(1-3\gamma)/2} t^{3(1-\gamma)} \dot{\mathcal{M}}_{\text{acc}}(x). \quad (\text{A12})$$

Mass loss rate due to outflows:

$$\dot{M}_{\text{w}}(r, t) = K^{3/2} G^{(1-3\gamma)/2} t^{3(1-\gamma)} \dot{\mathcal{M}}_{\text{w}}(x). \quad (\text{A13})$$

Mass loss per unit area (from Eq. 5):

$$\dot{\sigma}_{\text{w}}(r, t) = (4\pi)^{-1} K^{1/2} G^{-(1+\gamma)/2} t^{-\gamma-1} \Sigma(x) \Gamma(x). \quad (\text{A14})$$

Auxiliary dimensionless functions:

$$J(x) = x V_\phi(x), \quad (\text{A15})$$

$$\mathcal{M}_x(x) = \int_0^x \Sigma(x') x' dx', \quad (\text{A16})$$

$$\dot{\mathcal{M}}_{\text{w}}(x) = \int_0^x \Sigma(x') \Gamma(x') x' dx', \quad (\text{A17})$$

$$\dot{\mathcal{M}}_{\text{acc}}(x) = \frac{\Sigma x v_r}{3\gamma - 4}, \quad (\text{A18})$$

$$\Gamma(x) = (4\pi)^{(\gamma-1)/\gamma} \gamma^{-1/\gamma} \Sigma^{2(1-\gamma)/\gamma}(x) \Lambda(x), \quad \Lambda(x) = \Sigma V_z^+(x). \quad (\text{A19})$$

B. DISK GRAVITATIONAL FIELD

Basu (1997) estimated that the gravitational collapse of a magnetized cloud core with supercritical mass-to-flux ratio leads to a surface density profile:

$$\sigma(r) = \frac{\sigma_0}{\sqrt{1 + (r/R)^2}}, \quad (\text{B20})$$

where σ_0 is the central surface density and R is the instantaneous size of a central plateau of surface density. The asymptotic ($r \gg R$) form of this profile is $\propto r^{-1}$.

According to Toomre (1963), the gravitational field of a thin disk with surface density profile $\sigma(r)$ is

$$g_{\text{disk}}(r) = -2\pi G \int_0^\infty dr' r' \sigma(r') M(r, r'), \quad (\text{B21})$$

where

$$\begin{aligned} M(r, r') &= \frac{2}{\pi} \frac{d}{dr} \left[\frac{1}{r_{>}} K \left(\frac{r_{<}}{r_{>}} \right) \right], \\ r_{<} &= \min(r, r'), \\ r_{>} &= \max(r, r'), \end{aligned} \quad (\text{B22})$$

and K is the complete elliptic integral of the first kind. Integrating equation (B21) yields the gravitational field that corresponds to the surface density of the protostellar disk. For the profile given by Eq. (B20) the gravitational field is

$$g_{\text{disk}}(r) = \frac{-2\pi G \sigma_0 r}{(r^2 + R^2)^{1/2} \left[1 + \sqrt{1 + \left(\frac{r}{R} \right)^2} \right]}, \quad (\text{B23})$$

as in Basu (1997). The asymptotic form ($r \gg R$) of this profile is

$$g_{\text{disk}}(r) = -\frac{2\pi G \sigma_0 R}{r}. \quad (\text{B24})$$

Integrating Eq. (B20) yields an enclosed mass within a radius r equal to

$$M(r) = 2\pi\sigma_0 R^2 \left[\sqrt{1 + \left(\frac{r}{R} \right)^2} - 1 \right], \quad (\text{B25})$$

which has asymptotic ($r \gg R$) form

$$M(r) = 2\pi\sigma_0 R r. \quad (\text{B26})$$

Comparing Eq. (B24) and Eq. (B26), the asymptotic gravitational field can be written as

$$g_{\text{disk}}(r) = -\frac{GM(r)}{r^2}. \quad (\text{B27})$$

This partially justifies our model assumption in Eq. (2) that the gravitational field of the thin disk can be written in the same way as for a spherical mass distribution. However, a disk generally does not have a gravitational field that behaves in the same way as that of spherical object. The net gravitational field is determined by matter from both interior and exterior to a radius r . Power-law profiles $\sigma \propto r^{-p}$ with $p < 2$ yield gravitational fields that can be approximated by Eq. (B27), and there is an exact match when $p = 1$ as shown above. In our models presented in this paper we generally find $p \simeq 1.4$. Hence we explore this case numerically below.

A surface density profile generalized from Eq. (B20) is

$$\sigma(r) = \frac{\sigma_0}{\sqrt{1 + (r/R)^n}}, \quad (\text{B28})$$

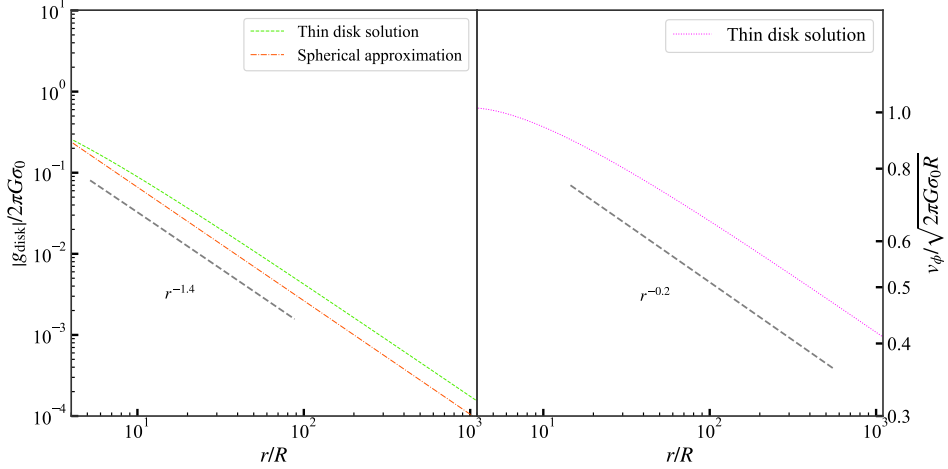


Figure B1. Left: The radial profiles of the normalized gravitational field g_{disk} for the numerical solution for a thin disk using Eq. (B21) and by using the spherical approximation $g_{\text{disk}} = -GM(r)/r^2$. Right: Normalized tangential velocity v_ϕ radial profile calculated from our numerical solver for the thin-disk model (see Eq. B21). Regions at larger radii follow a radial profile $\propto r^{-0.2}$, which is in excellent agreement with the self-similar model presented in this study. The surface density σ follows Eq. (B28) with $n = 2.8$.

where n can have different values. We choose $n = 2.8$ so that the asymptotic profile $\propto r^{-1.4}$. We solve for the gravitational field using Eq. (B21) by applying the methods described in Morton et al. (1994) and Basu & Mouschovias (1994). The asymptotic form of the calculated gravitational field is

$$g_{\text{disk}}(r) \propto r^{-1.4}, \quad (\text{B29})$$

Using the numerical solution for g_{disk} in the relation

$$\frac{v_\phi^2}{r} = -g_{\text{disk}}, \quad (\text{B30})$$

we find that

$$v_\phi \propto r^{-0.2}. \quad (\text{B31})$$

Figure B1 showcases the radial profiles of the normalized gravitational field and tangential velocity numerically calculated for the thin-disk model with a surface density having an asymptotic radial profile $r^{-1.4}$. Both the numerically calculated profiles match the radial profiles extracted from the solutions of the self-similar model (Figures 1- 4). These profiles are shallower than the Keplerian radial profiles observed with systems dominated by a central stellar mass. We also compare the gravitational field using a spherical approximation (assumed in Eq. 2) with the thin disk solution. The two differ on average by a small factor of $\simeq 1.5$, with the thin-disk field being stronger since all of the mass is in the plane of the disk.